npj | quantum information

Article

Published in partnership with The University of New South Wales

https://doi.org/10.1038/s41534-026-01295-y

Gradiometric, fully tunable C-shunted flux qubits

B. Berlitz[1] ✉, A. Händel[1], E. Daum[1], A. V. Ustinov[1,2] & J. Lisenfeld[1]

Fully tunable flux qubits offer in-situ and independent controls of their energy potential asymmetry and tunnel barrier, making them versatile tools for quantum computation and the study of decoherence sources. However, only short coherence times have been demonstrated so far with this type of qubit. Here, we present a capacitively shunted flux qubit featuring improved relaxation times up to $T_1 = 25\,\mu$s and a 20-GHz wide theoretical frequency tunability range at the flux-insensitive sweet spot, of which a 3-GHz range was shown. As a model application, we demonstrate detection of two-level tunneling defects in a frequency range spanning one octave.

Superconducting micro-circuits have become a tremendous testbed to explore quantum coherence in electrically controlled solid-state systems. There are various types of superconducting qubits such as the charge, phase, and flux qubit, which differ by the degree of freedom that dominates their energy. While not as widely used as transmon qubits in current large-scale architectures[1,2], flux qubits, which offer a higher anharmonicity, have served as an important tool for research in superconducting quantum circuits over the past two decades.

The original flux qubit[3,4] consisted of a superconducting loop that is interrupted by three Josephson junctions, one of which has smaller critical current than the other two by a factor $0.5 < \alpha < 1$, which defines the Josephson energies E_J for one large junction and αE_J for the small junction (see Fig. 1a). It features a double-well potential whose asymmetry is controlled by an external flux Φ_T (see Fig. 1b). In early experiments, flux qubits were read out by measuring the flux through the qubit loop using a DC-SQUID in switching-current[5] or dispersive measurements[6], and were used to demonstrate two-qubit gates[7], access the ultra-strong coupling cavity QED regime[8,9], and multiplexed qubit readout[10].

The quantum coherence of flux qubits steadily improved over the past years. Bertet et al.[11] and Yoshihara et al.[12] reported T_1 times of 2–4 μs in early experiments, which were likely limited by strongly coupled readout-SQUIDs. Subsequently, longer T_1 times of 6–20 μs were reached by Orgiazzi et al.[13] and Stern et al.[14], by replacing the readout-SQUID with coplanar waveguide resonators and 3D cavities, respectively.

Another design improvement was the addition of a shunt-capacitor. While in early experiments using interdigitated capacitors by Steffen et al.[15] and Córcoles et al.[16], T_1 times were limited to 1–6 μs, Yan et al. demonstrated coherence times of $T_1 \approx 50$ μs, using larger square-plate shunt-capacitors[17]. With this breakthrough, which they attributed to reduced dielectric loss in their shunt capacitors and a reduction in the qubit persistent current, flux qubits reached similar coherence times as transmon qubits.

For the symmetric double-well potential at a magnetic flux bias of $\Phi_T = \Phi_0/2$, a flux qubit has minimum resonance frequency f_q and lowest dephasing due to flux noise being suppressed in first order. Phase coherence (T_2) quickly degrades away from the optimal flux bias point, and this severely limits the practically useful qubit tunability range. In a “fully tunable” or “gap-tunable" flux qubit, this is addressed by replacing the small junction with a DC-SQUID, thereby making the effective junction area ratio α tunable in-situ by an additional control flux Φ_B. This was first shown by Paauw et al.[18]. Soon after, Poletto et al. demonstrated operation in both the double-well flux qubit ($0.5 < \alpha < 1$) and the single-well phase qubit ($\alpha < 0.5$) regime [19]. This control of the qubit potential makes gap-tunable flux qubits attractive for different applications, such as quantum annealing[20,21], as couplers and computational qubits in quantum processors[22,23], for use in quantum metamaterials[24] and for microwave-free qubit manipulation[25]. Gap-tunable flux qubits are particularly well suited for investigating decoherence sources, since a single device can access both flux-like and phase-like operating regimes. Their wide tunability enhances the accessible range for coherence spectroscopy, where qubit relaxation serves as a probe of its electromagnetic environment to reveal interactions with parasitic circuit modes or with microscopic two-level-defects (TLS).

So far, balancing the enhanced qubit tunability with good qubit coherence has been proven to be difficult. Early gap-tunable designs exhibited T_1 times between 1.4 ns and 1.5 μs, which have been attributed to thermal noise[18], and dielectric loss[25], respectively. In a recent experiment using an asymmetric α-junction SQUID, Chang et al. reported T_1 times up to 8 μs [23], attributing this limit to dielectric loss. However, this approach limits the tuning range of the device (about 7 GHz was reported). Despite this significant improvement in energy relaxation, a gap-tunable flux qubit, which combines access to a wide α-range with a long T_1 time has not yet been achieved.

Here, we present a gap-tunable capacitively shunted flux qubit that is based on the design of Yan et al.[17], which combines the coherence of the

---

[1]Physikalisches Institut, Karlsruhe Institute of Technology (KIT), Karlsruhe, Germany. [2]Institute for Quantum Materials, Karlsruhe Institute of Technology (KIT), Karlsruhe, Germany. ✉e-mail: benedikt.berlitz@outlook.de

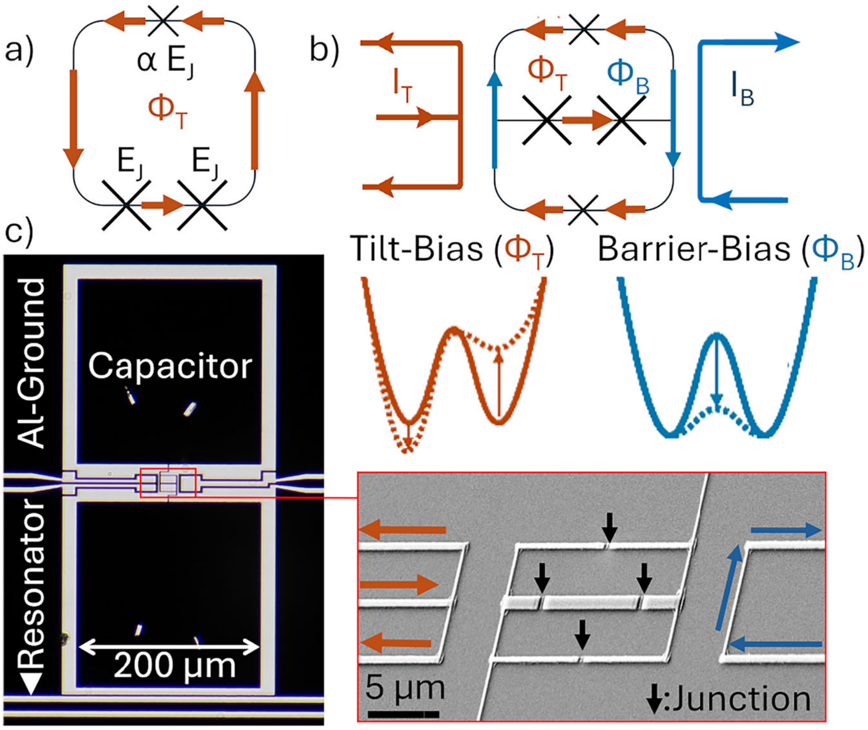

Fig. 1 | Sample design. a Idealized circuit diagram of a 3-Junction flux qubit, with one junction having a lower critical current by a factor of α. **b** Circuit diagram of a gradiometric fully tunable flux qubit. The currents (I_T, I_B) in the local bias lines induce the fluxes Φ_T and Φ_B, providing control of the potential asymmetry and barrier-height, respectively, which is illustrated by the orange and blue qubit potentials. **c** Micrograph of a fully tunable C-shunted flux qubit (sample A), with an inset zooming in on the junction layout under a 45° angle (corresponding area of sample B).

C-shunted flux qubit with wide tunability and in-situ α-control. Its half-gradiometric design provides independent local control of barrier and asymmetry-flux biases. We observed T_1 times up to 25 µs at 3.5 GHz, which corresponds to a qubit quality factor of $2\pi f_q \cdot T_1 \approx 500$k. Furthermore, we demonstrate strain-tuned TLS spectroscopy as a model application. This technique, previously implemented with phase and transmon qubits[26,27], demonstrates the suitability of our device for investigating microscopic defects in a wide frequency range. Taking advantage of this feature in future experiments could provide deeper insights into fundamental material properties such as the frequency dependence of the TLS state density, which is a central ingredient in defect models[28].

Results

Qubit tunability

To characterize the qubit tunability and the cross-talk between the two flux lines, we observe the dispersive shift of the readout resonator as a function of both applied flux biases. For this, a fast method is to only measure the transmission S_{21} at a fixed probe frequency f_{probe}[29]. As illustrated in Fig. 2a), the transmitted signal is minimal when the readout resonator resonance f_{res} equals the probe frequency. Since f_{res} depends on the qubit resonance frequency, this minimum indicates that the qubit was tuned to a certain frequency which depends on the chosen f_{probe}. The inside of the tear-shaped region in Fig. 2b thus corresponds to flux bias combinations where the qubit has lowest resonance frequencies. Due to crosstalk of the flux-bias lines, the uncalibrated measurement (top panel in Fig. 2b) is skewed. The lower panel shows the same measurement when the crosstalk is compensated by balancing the flux bias currents as further discussed in supplementary material E. Along the white line in the panels, the qubit potential has zero tilt $\Phi_T = 0$. Points of lowest and highest qubit frequency along this line are indicated by a star and triangle as in Fig. 2c.

After calibration, we measure the qubit energy relaxation time T_1 for a symmetric potential at different qubit frequencies by tuning the size of the potential barrier via the flux Φ_B.

Energy relaxation

Figure 3a shows that the qubit reaches an average quality factor $Q = 2\pi f_q\, T_1$ up to 530k at an operation frequency of 3.32 GHz, which corresponds to $T_1 \approx 25\,\mu$s. For this point, T_1 decay traces and Rabi oscillations are shown in Fig. 3b, c. We observe an increase in qubit coherence at lower qubit frequencies where the qubit potential crosses over into the double-well regime for $\alpha > 0.5$. This is explained by a combination of readout-resonator induced Purcell-loss and limitaton by ohmic charge noise, which has been shown to dominate the energy-relaxation of C-shunted flux qubits in this frequency range[17] (see supplementary material D for a discussion of loss mechanisms). The quality factor is comparable to that of transmon qubits (Q ~ 600k)[30] and quarton qubits (Q ~ 500k)[31] fabricated in the same facility.

TLS spectroscopy

The qubit's extended tunability makes it especially attractive to investigate TLS defects in a wide frequency range. A powerful method to study origins of decoherence is qubit swap spectroscopy[27,32], which reveals parasitic circuit modes and resonances of individual strongly-coupled TLS defects by minima in the frequency-dependent qubit T_1 time. With the ability to tune TLS by applied mechanical strain or DC-electric fields, one can measure spectral TLS densities and characterize the TLS' individual properties such as their coherence and dipole moment[26,33].

Figure 4 shows examples of TLS spectra that were acquired with the qubit operating in the single- or double-well regime. Both spectra span a similar strain and frequency range, while a larger number of TLS are visible at higher qubit frequencies. Such measurements allow one to probe the frequency-dependence of the TLS density of states, which can give clues about underlying microscopic defect mechanisms. This first strain-tuned TLS spectroscopy in a flux qubit demonstrates TLS-detection in a frequency range spanning almost one octave. It furthermore showcases the unique combination of fast, wide, and coherent frequency tuning our design provides. We note that the experimentally demonstrated tuning range is still a fraction of what is theoretically possible. In future experiments, using an optimized experimental setup, qubit operation spanning close to four decades (3 MHz - 21 GHz) could be achieved.

Discussion

In this work, we have presented a gap-tunable, capacitively shunted flux qubit featuring local flux biasing and a half-gradiometric geometry. We report coherence times up to T_1 = 25 µs (Q=500k) and demonstrate qubit

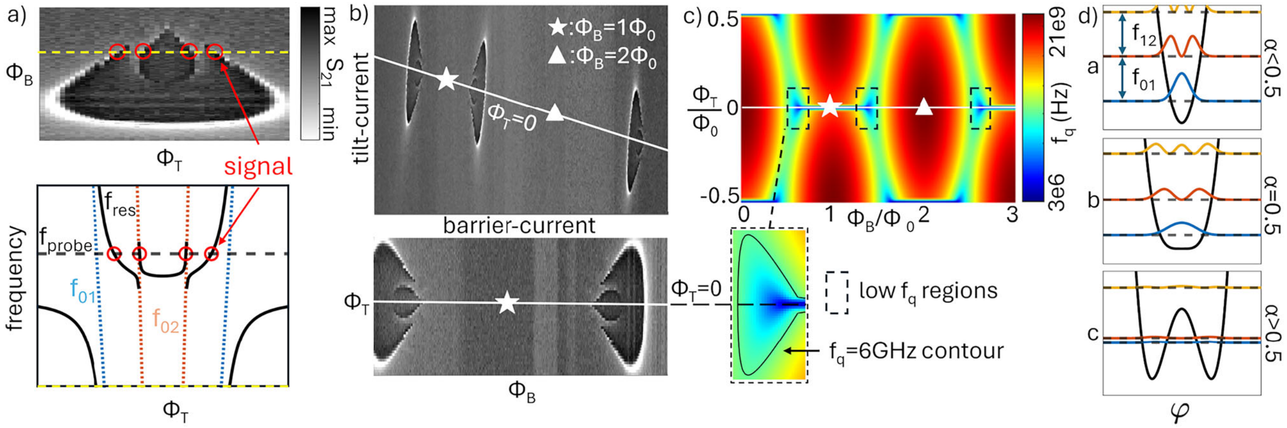

Fig. 2 | Qubit Calibration and tunability. a principle of a Φ_T-Φ_B-sweep calibration measurement. A signal (red circles) is detected, when f_{res} is shifted into resonance with f_{probe} by a qubit transition. **b** Calibration measurements used to identify symmetry points in the Φ_T-Φ_B-landscape and the bias line cross-talk (corrected in the bottom measurement). **c** Numerical calculation of the qubit resonance frequency f_q, spanning from 3 MHz to 21 GHz (linear scale). **d** Numerical calculation of the qubit potential for different α-values, including the 3 lowest qubit states. Shown measurements were performed on sample A.

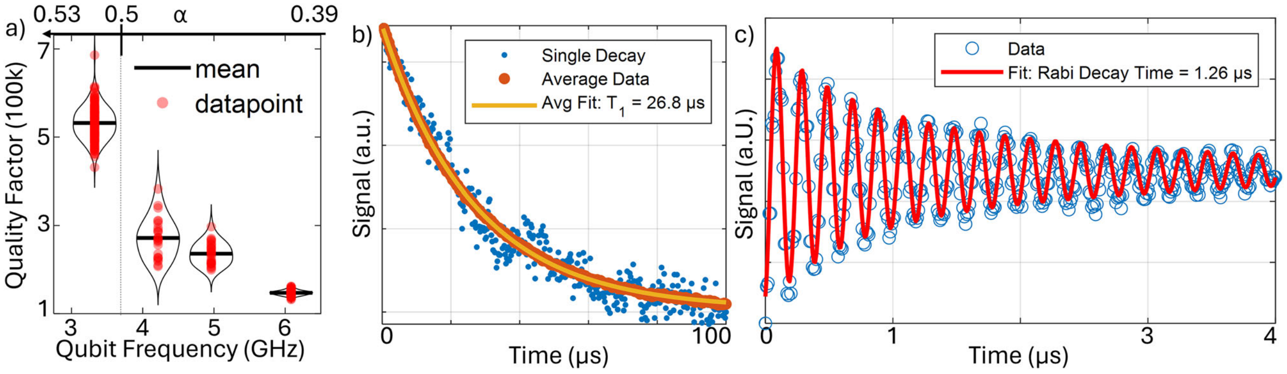

Fig. 3 | Energy Relaxation and Rabi measurements. a Violin- and scatter-plots of quality factor measurements at the potential symmetry point $\Phi_T = 0$ on sample A at different qubit frequencies, corresponding to different α-values at the cross-over into the double well regime ($\alpha > 0.5$), together with the theoretical limit (see Supplementary Material D). The mean quality-factors (from left to right) correspond to T_1 of 26.8 μs, 10.2 μs, 7.57 μs and 3.9 μs. **b** T_1-decay traces corresponding to the left-most violin. A single example trace is shown in blue and the average of all 150 traces taken over 8 hours is shown in red, with an exponential fit to the average trace in yellow. **c** Rabi oscillations measured at f_q=3.22 GHz.

frequency tunability spanning nearly an octave, with a close to four decade range theoretically possible. This design combines the advantages of high coherence with fast and wide frequency control, making it a promising platform for quantum material research and quantum information experiments.

As a model application, we have demonstrated strain-tuned TLS spectroscopy, showcasing the capability to probe TLS defects across a wide frequency range and in both the single- and double-well qubit regimes. These features are particularly valuable for future investigations into TLS density of states and defect classification schemes.

Beyond TLS spectroscopy, the combination of good coherence and broad tunability renders this design attractive for a wide range of applications. With advances in hybrid architectures[34–36], gap-tunable flux qubits could see use as intermediaries between high-frequency qubits and low-frequency quantum memories, where their wide tuning range could mitigate frequency crowding. The capability to quickly transition between single-well and double-well potential shapes enables alternative qubit operation schemes[25] and provides a unique testbed for studying decoherence mechanisms in distinct potential landscapes. The ability to couple via flux[37] and to implement strong ZZ-type interactions through barrier biasing[22] further underlines their versatility as building blocks for multi-qubit systems.

Methods

Sample details

Figure 1b, c shows a photograph of our gap-tunable flux qubit sample and its circuit schematic. It features two junctions of nominally equal critical current that are connected in a gradiometric loop via two smaller-area junctions whose critical currents are reduced by a factor $\alpha_{\text{max}}/2$.

The α-junctions act as a DC-SQUID whose critical current can be controlled by an applied homogenous magnetic flux Φ_B, effectively controlling the α factor in the qubit potential which is given by

$$U(\varphi) = -2E_J\cos(\varphi) - \alpha(\Phi_B)E_J\cos\left(2\pi\frac{\Phi_T}{\Phi_0} - 2\varphi\right), \qquad (1)$$

with E_J being the Josephson energy of one large junction and $\alpha(\Phi_B) = \alpha_{max}\cos(\pi\Phi_B/\Phi_0)$. Design values are chosen so that both the single-well ($\alpha < 0.5$) and the double-well ($\alpha > 0.5$) regime can be reached, which is illustrated in Fig. 2d. The asymmetry of the qubit potential depends on the difference flux Φ_T in the two loop branches which is controlled by a current-dividing flux bias line shown in Fig. 1b, c.

Figure 2c shows a numerical simulation of the qubit frequency as a function of the applied flux biases, where stars and triangles respectively

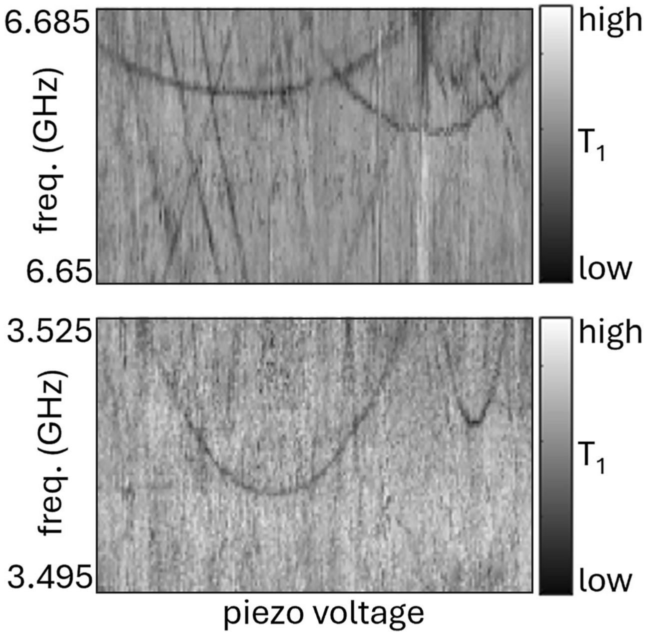

Fig. 4 | TLS-spectra in dependence of mechanical strain applied via a piezo-electric element. Dark lines indicate a drop in T_1 caused by resonant TLS defects. Spectra were taken on sample B with similar strain ranges for different frequency intervals.

indicate the lowest ($\Phi_B = 1\Phi_0$) and highest ($\Phi_B = 2\Phi_0$) qubit frequency for a symmetric qubit potential ($\Phi_T = 0$). The broad control over the qubit potential allows access to f_q tunability ranging from 3 MHz to 21 GHz.

The qubit population is controlled with resonant microwave pulses sent via the transmission line, while its state is read out by measuring the dispersive resonance shift of a capacitively coupled $\lambda/2$ readout-resonator.

Fabrication and experimental setup

The qubit samples are fabricated from aluminum on a sapphire substrate, using optical lithography and dry etching to pattern resonators and the qubit capacitor. The bias lines are deposited together with the Al-AlOx-Al junctions in a successive e-beam lithography step to ensure precise alignment. This reduces unwanted bias-line crosstalk. The junctions are made in a three-angle shadow evaporation process using a Dolan bridge[30] which avoids the formation of unwanted stray junctions, see supplementary material C for further details. Here, we present data from two samples, whose design parameters are detailed in Supplementary Material B. All measurements were performed at millikelvin temperature in a dilution refrigerator, whose setup is detailed in Supplementary Material A.

Data availability

Data and related scripts are available here: https://doi.org/10.5281/zenodo.18862873. Data analysis was performed using MATLAB2023b.

Code availability

Data and related scripts are available here: https://doi.org/10.5281/zenodo.18862872. Data analysis was performed using MATLAB2023b.

Received: 25 September 2025; Accepted: 29 May 2026;

References

1. AI, G. Q. & Collaborators. Quantum error correction below the surface code threshold. *Nature* **638**, 920–926 (2025).
2. Arute, F. et al. Quantum supremacy using a programmable superconducting processor. *Nature* **574**, 505–510 (2019).
3. Orlando, T. P. et al. Superconducting persistent-current qubit. *Phys. Rev. B* **60**, 15398–15413 (1999).
4. Mooij, J. E. et al. Josephson persistent-current qubit. *Science* **285**, 1036–1039 (1999).
5. Chiorescu, I., Nakamura, Y., Harmans, C. J. P. M. & Mooij, J. E. Coherent quantum dynamics of a superconducting flux qubit. *Science* **299**, 1869–1871 (2003).
6. Lupaşcu, A., Driessen, E. F. C., Roschier, L., Harmans, C. J. P. M. & Mooij, J. E. High-contrast dispersive readout of a superconducting flux qubit using a nonlinear resonator. *Phys. Rev. Lett.* **96**, 127003 (2006).
7. De Groot, P. et al. Selective darkening of degenerate transitions demonstrated with two superconducting quantum bits. *Nat. Phys.* **6**, 763–766 (2010).
8. Fedorov, A. et al. Strong coupling of a quantum oscillator to a flux qubit at its symmetry point. *Phys. Rev. Lett.* **105**, 060503 (2010).
9. Niemczyk, T. et al. Circuit quantum electrodynamics in the ultrastrong-coupling regime. *Nat. Phys.* **6**, 772–776 (2010).
10. Jerger, M. et al. Frequency division multiplexing readout and simultaneous manipulation of an array of flux qubits. *Appl. Phys. Lett.* **101**, 042604 (2012).
11. Bertet, P. et al. Dephasing of a superconducting qubit induced by photon noise. *Phys. Rev. Lett.* **95**, 257002 (2005).
12. Yoshihara, F. O. Decoherence of flux qubits due to 1/*f* flux noise. *Phys. Rev. Lett.* **97**, 167001 (2006).
13. Orgiazzi, J.-L. et al. Flux qubits in a planar circuit quantum electrodynamics architecture: Quantum control and decoherence. *Phys. Rev. B* **93**, 104518 (2016).
14. Stern, M. et al. Flux qubits with long coherence times for hybrid quantum circuits. *Phys. Rev. Lett.* **113**, 123601 (2014).
15. Steffen, M. et al. High-coherence hybrid superconducting qubit. *Phys. Rev. Lett.* **105**, 100502 (2010).
16. Córcoles, A. D. et al. Protecting superconducting qubits from radiation. *Appl. Phys. Lett.* **99**, 181906 (2011).
17. Yan, F. et al. The flux qubit revisited to enhance coherence and reproducibility. *Nat. Commun.* **7**, 12964 (2016).
18. Paauw, F. G., Fedorov, A., Harmans, C. J. P. M. & Mooij, J. E. Tuning the gap of a superconducting flux qubit. *Phys. Rev. Lett.* **102**, 090501 (2009).
19. Poletto, S. et al. A tunable RF squid manipulated as flux and phase qubits. *Phys. Scr.* **2009**, 014011 (2009).
20. Johnson, M. W. et al. Quantum annealing with manufactured spins. *Nature* **473**, 194–198 (2011).
21. Saida, D., Hidaka, M., Imafuku, K. & Yamanashi, Y. Factorization by quantum annealing using superconducting flux qubits implementing a multiplier Hamiltonian. *Sci. Rep.* **12**, 13669. https://doi.org/10.1038/s41598-022-17867-9 (2022).
22. Zhu, X., Kemp, A., Saito, S. & Semba, K. Coherent operation of a gap-tunable flux qubit. *Appl. Phys. Lett.* **97**, 102503 (2010).
23. Chang, T., Cohen, T., Holzman, I., Catelani, G. & Stern, M. Tunable superconducting flux qubits with long coherence times. *Phys. Rev. Appl.* **19**, 024066 (2023).
24. Shulga, K. V. et al. Magnetically induced transparency of a quantum metamaterial composed of twin flux qubits. *Nat. Commun.* **9**, 150 (2018).
25. Poletto, S. et al. Coherent oscillations in a superconducting tunable flux qubit manipulated without microwaves. *N. J. Phys.* **11**, 013009 (2009).
26. Lisenfeld, J. et al. Decoherence spectroscopy with individual two-level tunneling defects. *Sci. Rep.* **6**, 23786. https://doi.org/10.1038/srep23786 (2016).
27. Lisenfeld, J. et al. Electric field spectroscopy of material defects in transmon qubits. *npj Quantum Inf.* **5**, 105 (2019).
28. Müller, C., Cole, J. L. & Lisenfeld, J. Towards understanding two-level-systems in amorphous solids: insights from quantum circuits. *Rep. Prog. Phys.* **82**, 124501 (2019).

29. Quintana, C. *Superconducting flux qubits for high-connectivity quantum annealing without lossy dielectrics*. Ph.D. thesis, University of California, Santa Barbara, Santa Barbara, CA, USA (2017). https://escholarship.org/uc/item/9844c3h3. Ph.D. thesis; Advisor: John M. Martinis.
30. Bilmes, A., Händel, A. K., Volosheniuk, S., Ustinov, A. V. & Lisenfeld, J. In-situ bandaged Josephson junctions for superconducting quantum processors. *Superconduct. Sci. Technol.* **34**, 125011 (2021).
31. Kreuzer, A. Quarton qubits with stacked Josephson junctions. Ph.D. thesis, Karlsruher Institut für Technologie (KIT) (2026).
32. Barends, R. & others. Coherent Josephson qubit suitable for scalable quantum integrated circuits. *Phys. Rev. Lett*. **111**, 080502 (2013).
33. Hung, C.-C. et al. Probing hundreds of individual quantum defects in polycrystalline and amorphous alumina. *Phys. Rev. Appl.* **17**, 034025 (2022).
34. Zhu, X. et al. Coherent coupling of a superconducting flux qubit to an electron spin ensemble in diamond. *Nature* **478**, 221–224 (2011).
35. Reagor, M. et al. Quantum memory with millisecond coherence in circuit QED. *Phys. Rev. B* **94**, 014506 (2016).
36. Milul, O. et al. Superconducting cavity qubit with tens of milliseconds single-photon coherence time. *PRX Quantum* **4**, 030336 (2023).
37. van der Ploeg et al. Controllable coupling of superconducting flux qubits. *Phys. Rev. Lett.* **98**, 057004 (2007).

Acknowledgements

We thank Alexander Bilmes and Hannes Rotzinger for fruitful discussions, as well as for their contributions to the experimental setup and qubit fabrication. We thank Lucas Radtke and Silvia Diewald for their contributions to the fabrication. We are grateful for the clean room facilities provided for the fabrication by the Nanostructure Service Laboratory (NSL) at KIT. We acknowledge funding from the Baden-Württemberg Stiftung gGmbH (project QuMaS) and Google. The funders played no role in study design, data collection, analysis and interpretation of data, or the writing of this manuscript.

Author contributions

B.B. designed, fabricated and measured the qubits, analyzed the data and wrote the manuscript text. A.H. contributed to the fabrication procedures. E.D. contributed to qubit measurement and manuscript revision. A.U. contributed the laboratory, funding, and reviewed the manuscript. J.L. devised the study idea, supervised the entire process and reviewed the manuscript.

Funding

Open Access funding enabled and organized by Projekt DEAL.

Competing interests

The authors declare no competing interests.

Additional information

Supplementary information The online version contains supplementary material available at https://doi.org/10.1038/s41534-026-01295-y.

Correspondence and requests for materials should be addressed to B. Berlitz.